

Evaluating System-Level Fidelity with Peaked Random Circuits

Martin Brieger*, Florian Krötz*, Minh Chung*[†], Dieter Kranzlmüller*[†]

*Ludwig-Maximilians-Universität München (LMU), Munich, Germany
Email: m.brieger@campus.lmu.de, florian.kroetz@nm.ifi.lmu.de

[†]Leibniz Supercomputing Centre (LRZ), Garching, Germany
Email: {minh.chung, dieter.kranzlmueLLer}@lrz.de

Abstract—Quantum computing is transitioning from experimental prototypes to commercially available turnkey systems, making architecture-agnostic performance metrics essential for cross-platform comparison. Peaked Random Circuits (PRCs) have recently been proposed as a viable path to demonstrate quantum advantage on NISQ devices: a quantum processor can reliably detect a single, peaked output state amid background noise, yet the circuits’ characteristics render classical simulation infeasible. In this paper, we repurpose PRCs as a system-level fidelity benchmark. By successively running a matrix of PRCs with varying qubit counts and circuit depths, we quantify a system’s ability to identify the deterministic peak despite cumulative noise, gate errors, and connectivity constraints. We apply the benchmark on IQM’s superconducting and AQT’s trapped-ion architectures. Our results show that PRCs provide a high-precision metric comparable to Quantum Volume while exhibiting greater sensitivity to interference effects. Consequently, PRCs enable a robust framework for assessing the computational reliability of NISQ hardware across platforms.

Index Terms—Peaked Circuits, Random Circuits, Quantum Volume, Benchmarking, Fidelity, IQM, AQT

I. INTRODUCTION

The rapid expansion of the quantum computing landscape has fostered a diverse ecosystem of commercial backends, spanning modalities ranging from superconducting [1], trapped-ion [2], and neutral-atom [3] to photonic [4] quantum computers. As hardware architectures diverge, the necessity for architecture-agnostic performance metrics becomes critical. Traditional benchmarks often struggle to capture the nuances of system-level fidelity—the holistic ability of a machine to maintain coherence and gate accuracy during complex executions—across these heterogeneous platforms.

In this paper, we propose a benchmarking methodology based on Peaked Random Circuits (PRCs). Originally conceptualized by Aaronson and Zhang to demonstrate Quantum Advantage [5], [6], PRCs are structured, quasi-random circuits designed to produce a predictable output distribution dominated by a single “peak” state. Ideally, one specific bitstring is observed with high probability, while the remaining probability mass is distributed uniformly across all other outcomes. While PRCs can, in principle, demonstrate a quantum advantage of today’s devices—the idea being that the task of identifying the peak bitstring is easy to run and verify while

the circuits are classically hard to simulate—this work adapts them for system-level benchmarking.

By running a set of PRCs on hardware with a known target bitstring, we can directly quantify fidelity. First, by the machine’s ability to identify the peak and second by the measured contrast between the peak and the surrounding “noise floor”. Accordingly, we introduce Peak Identification and Fidelity Error (\mathcal{F}) as evaluation metrics; the latter provides a transparent view of how hardware noise blurs the results. Computing these metrics across a matrix of circuits with varying qubit counts and depths probes the device’s capability boundary.

Because they capture high-resolution noise effects, our metrics expose details that aggregate standards fail to resolve. In contrast to the industry-standard Quantum Volume (QV) [7], PRCs offer three distinct benefits for evaluating heterogeneous systems:

- 1) *Efficient Verification*: QV requires exponentially expensive classical simulation to identify “heavy outputs”. The success of peak identification can be verified instantaneously, avoiding the bottleneck of classical computation.
- 2) *High Signal-to-Noise Ratio*: QV measures a statistical distribution of many output states. In contrast, PRCs concentrate probability on a single, sharp peak, creating a clearer contrast between the intended signal and the underlying hardware noise.
- 3) *Architectural Flexibility*: QV mandates “square” circuits with the number of qubits matching the circuit depth. PRCs decouple these parameters, enabling independent stress tests of a system’s width (scalability) and its depth (coherence time).

The core contributions of this work are threefold. First, we repurpose Peaked Random Circuits (PRCs) as a system-level, architecture-agnostic benchmark, extending their original application to a universal performance-assessment framework. Second, we introduce tailored evaluation metrics that accurately capture the distinctive performance aspects of PRCs, such as peak-recovery fidelity and sensitivity to interference. Third, we validate our methodology across platforms by conducting extensive experiments on two commercial quantum

computers: a superconducting system from IQM [8] and a trapped-ion system from AQT [9].

The remainder of this paper is organized as follows: Section II summarizes related works and established quantum benchmarking methods. Section III provides the theoretical background on PRCs and our adaptation toward a new benchmarking framework for quantum computers. In Section IV, we introduce the benchmarking pipeline and formally define our evaluation metrics. Section V describes the experimental setup, detailing the architectural specifications, while Section VI presents the empirical results and discussion. Finally, in Section VII, we conclude the paper and outline potential future works.

II. RELATED WORK

A range of benchmarking methods and frameworks has been proposed to characterize the performance of NISQ devices, each emphasizing different aspects of hardware quality [10]–[12]. At the system level, *Quantum Volume* (QV) has become a common metric for comparing quantum processors, as it captures the largest random-square circuit a device can successfully execute under a heavy-output criterion [13]. However, QV compresses device performance into a single scalar and may not fully reflect how structured interference patterns degrade under realistic noise and connectivity constraints [7]. *CLOPS* complements QV by quantifying execution throughput in terms of circuit layer operations per second, but it primarily measures speed rather than computational fidelity [14], [15]. These metrics are therefore useful for broad comparison, yet they provide only a partial view of end-to-end computational reliability. Besides, QV and CLOPS are also analyzed as the benchmarks based on the efficiency of executing a specific type of circuits. Following this, QLOPS is more clearly defined for general quantum algorithms [16].

At a lower level, *Randomized Benchmarking* (RB) remains a standard tool for estimating average gate errors [17], [18]. RB is primarily used to characterize one- and two-qubit operations, but it is not designed to probe the cumulative effects of qubit mapping as well as connectivity limitations in larger multi-qubit circuits. Other approaches, such as using mirror circuits for scalable randomized benchmarking, extend this idea to deeper and wider circuits by constructing invertible circuit instances that ideally return the system to a known output state [19]. These methods improve scalability for system-level characterization but still primarily focus on recovering the mirrored structure for flexible randomized benchmarking of Clifford gates rather than prioritizing the high-probability outcomes necessary to probe signal integrity above noise.

At the application-oriented or algorithmic level, many studies focus on benchmarking quantum hardware through reference workloads such as variational algorithms, search routines, or chemistry-inspired circuits [20], [21]. These benchmarks are valuable because they reflect end-to-end behavior in realistic use cases, but their results can depend strongly on the chosen workload, compilation strategy, and hardware-specific optimizations.

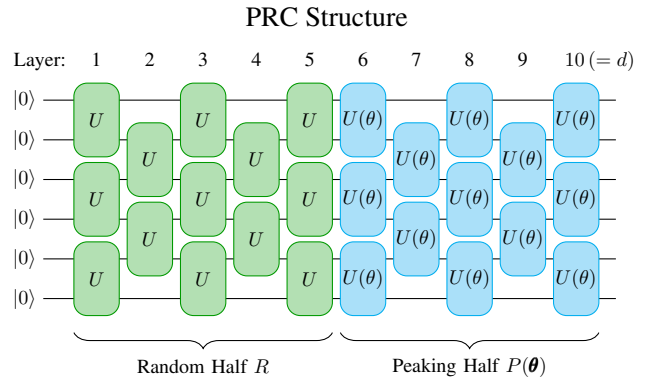


Fig. 1. Mirror architecture of the Peaked Random Circuits (PRCs) we use for benchmarking. The green and blue rectangles illustrate two-qubit unitary gates. We refer to the total number of layers as the circuit’s depth d .

In this paper, we use *Peaked Random Circuits* (PRCs) [5], [6] to provide a more architecture-independent stress test of computational fidelity. By examining whether and “how well” a device can preserve a deterministic output peak as circuit depth and qubit count increase, PRCs directly probe the system’s ability to maintain the interference structure required for reliable quantum computation across different hardware platforms.

III. PEAKED RANDOM CIRCUITS FOR SYSTEM-LEVEL BENCHMARKING

A. Structure

We use a mirror-circuit architecture described in the foundational PRC papers [5], [6]. This approach builds on the fact that any mirrored, unitary circuit $U^\dagger U$ is trivially peaked at the input register.

The construction of n -qubit circuits with depth d consists of three steps. First, we generate $d/2$ layers of random two-qubit unitary gates and arrange them in a $1D$ brick-wall pattern, forming the “random half” of the circuit, denoted R . Second, we append another $d/2$ layers of randomly generated two-qubit unitaries, which form the “peaking half” $P(\theta)$ and result in a structurally mirrored circuit $C = P(\theta)R$. Third, the gate-parameters θ of the peaking half are optimized numerically to maximize the expected value of the output bitstring s given the all-zero input register:

$$\max_{\theta} |\langle s | RP(\theta) | 0^n \rangle|^2. \quad (1)$$

Conceptually, the random half distributes the probability mass uniformly across the state space, while the peaking half concentrates it on the target bitstring. Figure 1 illustrates the PRC architecture. The circuit’s n qubits are represented by horizontal lines, intersected by a sequence of two-qubit unitary gates that strictly connect their neighboring qubits, depicted as green and blue rectangles. Each layer of gates is offset from the next, forming a brick-wall pattern that ensures full entanglement across the register over time.

When PRCs are executed on a quantum processor for a given number of shots, we expect s to be the most frequent

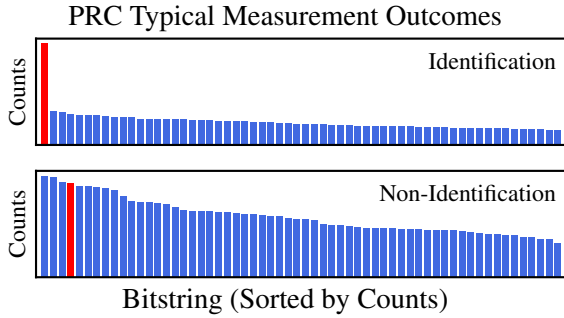


Fig. 2. Typical output histograms of PRCs obtained from several runs on a quantum device. The bar heights represent the frequencies of the measured bitstrings. The target bitstring is highlighted in red. In the upper panel, the most frequent result matches the target bitstring, illustrating *identification*. In the lower panel, a different bitstring peaks, demonstrating *non-identification*.

outcome. We refer to this result as *identification*. Conversely, *non-identification* occurs when s is not the dominant sample. Figure 2 exemplifies the two events with typical outcome histograms.

B. Generating Benchmark Circuits

To align with the capabilities of the devices under benchmark, we constructed a matrix of PRCs spanning a register size of $n \in [2, 20]$ qubits and circuit depths $d \in [2, 50]$. For odd-depth circuits, we shortened the depth of the random half to $d/2 - 1$. We found that a more skewed random-to-peaking layer ratio either diminishes the peak probability achievable within a fixed optimization period or requires additional runtime to achieve the desired peakedness. The two-qubit circuits present an edge case: as their register size cannot accommodate the alternating brick-wall layout, their gates are aligned sequentially.

Building on the source code released with the foundational papers, we represented the circuit as a tensor network and optimized it using the quimb library in Python. A hybrid optimization scheme, comprising 5,000 iterations of the L-BFGS-B algorithm followed by 10,000 iterations of the Adam optimizer, resulted in an ideal trade-off between maximizing peak probability and maintaining computational tractability.

The default behavior of the circuits is to concentrate probability on the all-zero bitstring. Any alternative peak can be realized by inserting NOT gates into the last layer and fusing them with the neighboring two-qubit unitaries. To determine whether this modification affects our performance metrics, we created a set of 10-qubit PRCs whose peak bitstrings are multiples of 00, 01, 10, and 11. Each circuit-bitstring pair was executed five times on our target devices. The results showed no discernible variation, prompting us to keep the default.

C. Difficulty

The difficulty of any quantum-computational task is fundamentally tied to the circuit size: larger registers and deeper gate sequences require higher fidelity and stronger coherence to execute successfully.

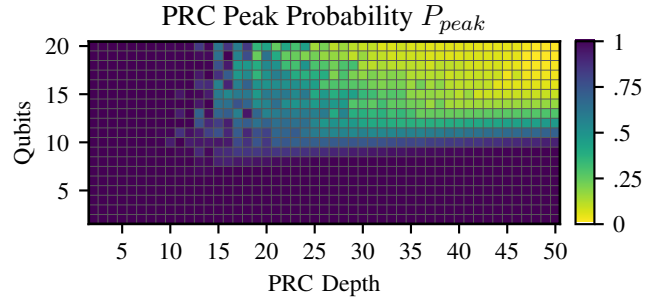


Fig. 3. Probability of the circuit to output the target, peak bitstring of our set of 931 PRCs by their number of qubits and depth. The values correspond to the results obtained in the optimization phase of circuit generation.

For PRCs, an increase in depth is accompanied by a rapid growth of entanglement originating from the brick-wall structure: every added layer of two-qubit gates entangles qubits across the entire lattice. Even a single-layer increment introduces new entangling bonds that will stress the devices' coherence times and gate-fidelity budgets.

Figure 3 quantifies how this scaling manifests in the peak probability P_{peak} of the benchmark circuits. As the number of qubits and the depth increase, the achieved probability mass on the peak bitstring decreases. This relationship is intrinsic to the PRC design and results from performing the optimization in a single step. Larger circuits require optimizing more parameters, which increases the computational cost and reduces the attainable peak probability.

To scale PRC generation, it has been proposed to use a discrete circuit design that sequentially optimizes independent blocks of gates [22] or embed a circuit reminiscent of the identity between the random and peaking half [23]. However, we favor the simple brick-wall construction of the mirror design as it yields a dense entangling pattern and a uniform gate distribution. This uniformity is beneficial for benchmarking: it guarantees that every qubit participates equally in the dynamics of execution, prevents hidden locality shortcuts, and makes the difficulty attributable to the overall size and entanglement rather than to architecture-specific factors. Moreover, even an ideal PRC would still show declining peakedness as qubit count rises, since the total probability must be distributed over an exponentially growing output space.

A major concern with decreasing P_{peak} is that the benchmark becomes harder or even impossible to solve. If the difficulty of identifying the peak bitstring were biased by varying peak probability, the benchmark would no longer reflect the intended scaling by circuit size. We therefore must ensure that circuit size is the primary driver of difficulty. There are two considerations supporting this:

1) *Simulation*: The runtime required to simulate a circuit can serve as a proxy for its intrinsic difficulty, especially for PRCs that are intended to be harder to compute classically than to run on a quantum device. Using a Matrix Product State (MPS) backend, we simulated the full benchmark suite

and found that the task of bitstring identification remained tractable across all instances, with runtimes below one minute. Producing 1,000 samples is sufficient to correctly and reliably identify the peak bitstring of the largest 20-qubit circuit with a depth of 50 and a peak probability of only 0.41 percent. This result suggests that small values of P_{peak} do not significantly affect the benchmark’s tractability or difficulty.

2) *Peak Dominance*: A clean separation between the peak and the rest of the distribution is crucial for successful identification. We quantify Peak Dominance as:

$$\mathcal{R}_p = \frac{P_{peak}}{P_{second}} \quad (2)$$

where P_{peak} and P_{second} are the probabilities of the most- and second-most-likely bitstrings, respectively. A large \mathcal{R}_p guarantees that, given enough samples, the peak will stand out to be identified even when its absolute probability is low. Our simulation data show that the largest PRC has a Peak Dominance of $\mathcal{R}_p = 14$. In other words, the peak appears at least fourteen times more often than any competing outcome. Smaller circuits exhibit ratios in the thousands, indicating an even clearer separation. Consequently, the peaks of our circuits are pronounced enough to remain identifiable at all times, given that enough shots are produced. This evidence supports the conclusion that the decreasing peak probability likely does not affect either the benchmark’s tractability or its difficulty.

As will be shown in detail, the capability ceiling of our target NISQ hardware was reached at circuit sizes with peak probabilities in the double-digit percentage range and peak dominance in the hundreds, indicating that the diminishing peak probability does not dominate the benchmark’s difficulty.

Consequently, for the PRC benchmark, the driver of difficulty is the increase in qubit count and circuit depth, i.e., the growth of entanglement, whereas the reduction in peak probability remains a secondary effect that does not threaten the task’s tractability. Nevertheless, advancing towards the future benchmark standard for ever more capable hardware will demand a more scalable method for generating PRCs.

Finally, a meaningful benchmark must exhibit a deterministic, incremental increase in difficulty from one instance to the next. To enforce this, we generated a single, unoptimized reference circuit, similar in size to our largest circuit. Each smaller PRC is built from (part of) the reference circuit’s random half and peaking half, the latter serving as a common starting point for optimization. Despite having optimized and thereby varying gate parameters in the peaking half, the only systematic change from one circuit to the next is the addition of one qubit or one layer, hence a marginal, predictable increase in entanglement and, by extension, in computational difficulty. This design guarantees intra-circuit comparability across the entire benchmark suite.

IV. EVALUATION METRICS

To evaluate the computational capability of NISQ devices, metrics must account for gate errors, crosstalk, and connectivity constraints. The industry-standard Quantum Volume (QV)

is a statistical aggregate that can be insensitive to specific hardware pathologies. Because it pools the success of many states, a device might pass a QV test while struggling with algorithms that require high-precision constructive interference.

The PRC benchmarking pipeline is designed to progress from high-level system stress testing to granular fidelity analysis. Unlike aggregate statistical measures, our metrics focus on the “sharpness” of the result: the machine’s ability to distinguish a specific computational signal from the background noise floor.

A. Success Criteria: Peak Identification

To start with and to obtain a clear operational boundary for the hardware, we apply a binary Peak Identification check. In the event of identification, i.e., the target bitstring s being the most frequent outcome state in the experimental distribution, the test is passed. In the event of non-identification, i.e., the dominant outcome not matching s , the test fails.

B. Quantifying Sharpness: Relative Peakedness (C)

To measure “how well” a device is able to recover the peaked bitstring in case of successful identifications, we propose a Relative Peakedness metric $C_{exp} \in [0, 1]$, calculated as the normalized difference:

$$C_{exp} = \frac{\hat{P}_{peak} - \hat{P}_{second}}{\hat{P}_{peak} + \hat{P}_{second}}. \quad (3)$$

\hat{P}_{peak} corresponds to the peak probability and \hat{P}_{second} to the probability of the second most probable outcome, both obtained from the experimental distribution. $C = 1$ indicates a perfectly “sharp” peak that is clearly distinguishable from the strongest competing error state, whereas $C = 0$ indicates that the hardware can no longer differentiate the signal from the background noise.

Our metric corrects for the fact that the state space expands as 2^n with increasing qubit count n , causing the probability of any one basis state to vanish, including the peak. As \hat{P}_{peak} naturally falls with a growing register size, larger circuits could be penalized, regardless of hardware quality. The normalization ensures that the benchmark is a fair test of constructive interference rather than a measure of state-space sparsity.

C. Fidelity Error (\mathcal{F})

Our benchmark circuits have varying peak characteristics that need to be accounted for. If a perfect PRC with a peak probability of $P_{peak} = 1$ is run on an ideal quantum device, measurement outcomes would show a perfect result of $C_{exp} = 1$. In practice, a PRC with a less distinct peak, i.e., one that exhibits a low Peak Dominance \mathcal{R}_p and distributes some probability mass among competing outcomes, cannot achieve a perfect result even on an ideal device; the measurements will at best reflect the circuit’s weak peak profile rather than the device’s true capability. Consequently, a metric constructed for heterogeneous PRCs must both accurately measure a device’s ability to preserve signal integrity above noise and remain

TABLE I
SELECTED PRC PEAK CHARACTERISTICS

Qubits	Depth	P_{peak}	\mathcal{R}_p	C_{max}
5	10	0.9991	3840	0.9995
5	20	0.9992	10969	0.9998
5	30	0.9992	8210	0.9998
5	40	0.9991	9141	0.9998
5	50	0.9990	5585	0.9996
10	10	0.9251	503	0.9960
10	20	0.8398	557	0.9964
10	30	0.7285	291	0.9932
10	40	0.8325	474	0.9958
10	50	0.9083	1355	0.9985
15	10	0.9990	9990	0.9998
15	20	0.5910	328	0.9939
15	30	0.3382	338	0.9941
15	40	0.1108	139	0.9857
15	50	0.0913	152	0.9869
20	10	0.9877	898	0.9978
20	20	0.4170	199	0.9900
20	30	0.0936	234	0.9915
20	40	0.0499	166	0.9881
20	50	0.0041	14	0.8646

comparable across circuits. This requires normalizing Relative Peakedness by the best-case achievable value C_{max} .

We calculate this correction factor using the first- and second-peak probabilities P_{peak} and P_{second} obtained during circuit generation and used to construct \mathcal{R}_p . Scaling C_{exp} by C_{max} yields the Fidelity Error $\mathcal{F} \in [0, 1]$:

$$\mathcal{F} = 1 - \frac{C_{exp}}{C_{max}}. \quad (4)$$

The Relative Peakedness ratio expresses the “fidelity” with which a device recovers a circuit’s inherent peak sharpness. By taking the complement of the ratio, the metric becomes a measure of “fidelity error”: an \mathcal{F} value near 0 indicates that the target state remains clearly distinguishable from background noise (recognizing that perfect separation cannot be achieved). Conversely, an \mathcal{F} value close to 1 indicates that the hardware has lost the ability to differentiate the correct answer from the strongest error state, signaling a breakdown in system-level fidelity.

To illustrate typical peak profiles and the magnitude of correction required, Tab. I shows the peak probability P_{peak} , Peak Dominance \mathcal{R}_p , and Relative Peakedness C_{max} of representative benchmark PRCs, sorted by circuit size and rounded to four decimals. While larger circuits generally exhibit lower P_{peak} and \mathcal{R}_p , the Relative Peakedness C_{max} used for correction stays approximately one, except for the largest circuit. This indicates that, in practice, even sizable circuits retain sufficient peak sharpness for the device to recover, making the correction more of a technical refinement than an essential adjustment.

Our dual-metric approach ensures that we capture both the ordinal correctness (Was the bitstring recovered?) and the computational margin (How well was it recovered?).

V. EXPERIMENTAL METHODOLOGY

To evaluate the robustness of the PRC benchmarking protocol, we performed a cross-platform study using two commercial quantum systems with distinct physical modalities hosted at the Leibniz Supercomputing Centre (LRZ)¹ of the Bavarian Academy of Sciences.

A. Devices

The first system is a “Radiance” superconducting device from IQM (codename **QExa20**), comprising 20 qubits arranged in a square-lattice connectivity topology [8]. IQM advertises a Quantum Volume (QV) of at least 32 and provides the median fidelities and durations for single- and two-qubit gates, the median readout fidelity, and the maximum number of qubits that can be placed in a GHZ state with fidelity greater than 0.5.

The second system is a “Marmot” trapped-ion device from AQT (codename **AQT20**), also with 20 qubits but featuring all-to-all connectivity [9]. During our experiments, 16 of its qubits were functional. The device is promoted with a QV of 128 on a seven-qubit register, and AQT reports average single- and two-qubit error rates on an 11-qubit register together with nearest-neighbor crosstalk.

Relying solely on the manufacturers’ specifications makes it hard to assess the true performance of either system. Although both report a QV, the individual values cannot be directly compared and fail to capture the full range of each system’s capabilities. This underscores the necessity for a standardized, more nuanced performance metric.

B. Execution Pipeline

To ensure the benchmark is deterministic and fair for the two devices under test, we employ the following execution strategy:

1) *Deterministic Transpilation*: We first converted the circuits from their original tensor network representation to the OpenQASM format. Each execution then involved transpiling the circuit into the target device’s native gate set using the Qiskit transpiler [24], applying the appropriate translation and scheduling passes. Specifying a fixed optimizer seed guarantees that run-to-run variations are attributable to hardware performance rather than stochastic differences in the compilation process.

2) *Software Stack*: We interfaced with the LRZ quantum devices, submitted jobs, and monitored their execution using the Qiskit adapter included in the Munich Quantum Software Stack (MQSS) [25].

3) *Sampling Strategy*: We empirically determined the appropriate number of shots for each job. While 200 shots generally sufficed for the AQT20, we used a range of 10,000 to 1,000,000 shots for jobs on the QExa20, with larger circuits demanding more samples. A sensitivity analysis indicated that increasing the shot count beyond these values did not yield additional identifications.

¹<https://www.lrz.de/en/technologies/quantum-computing>

C. Benchmarking Protocol

Each circuit configuration, defined by qubit count q and depth d , was executed five times to account for temporal drift. Consequently, the reported metrics represent averages over these runs.

We used an adaptive execution strategy to optimize compute resources. For instance, the sequence of runs begins at the lowest circuit depth for each qubit count. If five consecutive circuits at increasing depths resulted in non-identifications, subsequent executions for that qubit count were skipped.

Typical job runtimes ranged between 5 and 300 seconds on both devices, depending on queue latency and device calibration cycles.

VI. RESULTS AND DISCUSSION

This section evaluates the experimental performance of the QExa20 (superconducting) and AQT20 (trapped-ion) systems. Our analysis focuses on the transition from successful identification to noise-dominated results as circuit volume increases.

A. Visualizing the Results

Fig. 4 shows the benchmark outcomes for both the Peak Identification and Fidelity Error metrics. QExa20 results are displayed in the top panel and AQT20 results in the bottom panel. Each plot is arranged as a two-dimensional grid whose horizontal axis corresponds to circuit depth d and vertical axis to the number of qubits q . Every cell on the $(d \times q)$ lattice is color-coded: a colored cell signals a successful peak identification, a light-gray cell indicates a failure to identify the peak, and a white cell marks a configuration that was not executed. A black line traverses the plots, separating the circuits that were actually run from those that were omitted. For the successful runs, the colormap reflects the Fidelity Error \mathcal{F} : a value close to zero means the target bitstring stands out clearly against the noise, whereas a value approaching one signals that the hardware can barely distinguish the peak from the dominant error state.

Jointly presenting the result matrices of multiple devices side by side transforms the PRC benchmark into a versatile, heterogeneous testbed. This format makes it easy to contrast systems built on different physical modalities, while the x- and y-axes can be freely adjusted to reflect each platform’s performance range and to streamline the comparison.

B. Operational Boundary

Comparing the colored cells in Fig. 4 to the white and gray background displays a clear operational boundary. Both devices could reliably detect the peak for modest-size circuits, yet QExa20 demonstrated a noticeably larger operational range: across the 5- to 16-qubit span, it consistently outperformed AQT20 in handling deeper PRCs.

The shape of the boundary reflects performance scaling. As circuit width increases, the maximum attainable depth generally declines, producing a diagonal contour. Nevertheless,

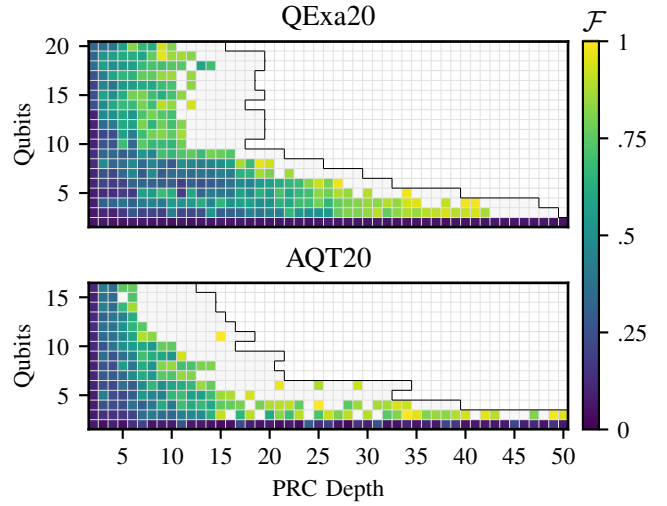


Fig. 4. Successful recoveries of the peaked bitstring by the circuits’ depth and number of qubits for the QExa20 superconducting device and the AQT20 ion-trap device. Colored cells indicate a matching peaked bitstring in at least three of five runs. Light-gray cells indicate non-identifications. White cells indicate skipped runs resulting from previously run, lower-depth circuits yielding non-identifications. The black line separates executed circuits from skipped ones. The colormap indicates the Fidelity Error \mathcal{F} .

QExa20 scales more favorably for larger registers, continuously supporting depth-10 circuits throughout the 10- to 20-qubit region.

The distribution of successful identifications serves as a proxy for performance consistency. Across the lattice, AQT20’s successes appear more erratic—occasionally an identification success follows a series of failures, and vice versa, indicating less stable performance. In contrast, QExa20’s identifications develop uniformly until the operational boundary is reached.

When binary success/failure outcomes are considered without regard to peak identification quality, QExa20 demonstrates higher overall performance, superior scaling, and greater consistency than AQT20.

C. Fidelity Error Analysis

The Fidelity Error \mathcal{F} , visualized by the color scale in Fig. 4, enables a deep diagnostic of the success matrices, providing a more granular view of hardware performance. By examining the transition zones where \mathcal{F} begins to climb from 0 to 1, we can distinguish between performance loss caused by adding more qubits (width) versus adding more gates (depth). This transition from a general “capability horizon” to a specific sensitivity analysis reveals that the breakdown of signal integrity is not uniform across different devices.

In both systems, the hardware’s ability to differentiate the target signal from background noise vanished as the computational volume $(d \times q)$ increased. However, the error rates were platform-dependent and heterogeneous, motivating a more detailed comparison.

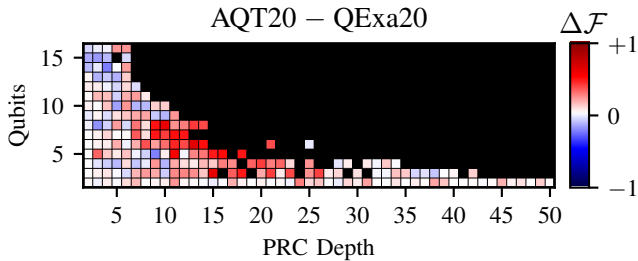


Fig. 5. Difference in the quality of peak identification between the AQT20 ion-trap device and the QExa20 superconducting device by the circuits’ depth and number of qubits. Colored cells indicate successful peak identifications of both devices. The colormap quantifies the difference in the Fidelity Error between the two devices: $\Delta\mathcal{F} = \mathcal{F}_{AQT20} - \mathcal{F}_{QExa20}$

Fig. 5 visualizes the difference in achieved Fidelity Error between the two devices, calculated as:

$$\Delta\mathcal{F} = \mathcal{F}_{AQT20} - \mathcal{F}_{QExa20}. \quad (5)$$

The data values were linearly mapped to a diverging colormap defined on the symmetric interval $[-1, 1]$, centered at zero. Blue-colored cells denote configurations where AQT20 outperforms QExa20 (lower error), while red-colored cells mark configurations where QExa20 is superior (higher error for AQT20). The axes remain consistent with the previous analysis. White cells indicate equal performance.

The presence of local, red, and blue “heat zones” on the lattice clearly shows that the devices’ performance scales differently with circuit width and depth. QExa20 outperforms the competitor in deep circuits with fewer qubits, achieving a higher peak separation for those configurations. In contrast, AQT20 excels with broader, shallower circuits, exhibiting a lower Fidelity Error than QExa20. However, this advantage is less striking, as reflected in fewer blue cells and lighter color saturation.

This analysis highlights the strength of our dual-metric approach. Although the operational boundary alone implies that QExa20 is categorically superior to AQT20, the Fidelity Error metric reveals a more nuanced picture: AQT20 offers a small yet measurable benefit in signal preservation for larger-register circuits with fewer gates.

D. Cross-Platform Comparison

Several observations emerge when evaluating performance across two distinct architectures:

1) *Connectivity and Topology*: All-to-all qubit connectivity can be beneficial for circuits that need long-range interactions, since it removes the need for additional routing gates that would deplete the error budget more rapidly. Our benchmark PRCs are built in a brick-wall pattern with each gate strictly coupling adjacent qubits; therefore, a chain connectivity is sufficient to execute the circuits without extra routing. The QExa20’s square-lattice topology can form such a chain, so it does not incur the penalty over the fully connected qubits of AQT20. We confirmed no connectivity bias exists

by performing a post-transpilation gate-count analysis: both devices executed exactly the same number of two-qubit gates for each circuit. In general, our PRC benchmark remains platform-agnostic as long as the hardware can realize a linear chain topology.

2) *Hardware-Specific Noise Pathologies*: On the QExa20 system, we observed signs of crosstalk in larger registers. As more qubits were utilized, the noise floor became increasingly non-uniform, with “ghost peaks” appearing near the target bitstring, likely due to localized coherent errors. AQT20 did not exhibit this effect, offering a plausible reason for its superior performance on those circuits.

3) *Physical Limits*: AQT20 encountered a physical limit at the $q15d15$ configuration, corresponding to 2000 native gates, beyond which the system returned gate-count errors. This limitation originates from the need to preserve stability in long ion chains and the duration of gate operations: AQT20’s performance horizon is hard-capped by the total number of operations the system can maintain before the chain requires re-cooling. In practice, the operational boundary was reached before the physical limit, so the performance assessment was not impaired.

4) *Modes of Failure*: Our experiments highlight two distinct failure modes in NISQ hardware. While our MPS simulations (discussed in Subsection III-C) recovered the peak for the largest 20-qubit, depth-50 circuit in under a minute, the physical devices faced a “precision vs. reach” trade-off. For AQT20, the challenge is maintaining the count of successful outcomes. For QExa20, the challenge is preventing the interference patterns from being buried by cumulative decoherence.

VII. CONCLUSION

We introduced a new benchmarking methodology based on Peaked Random Circuits (PRCs). Our method is architecture-agnostic and easy to verify without heavy classical computation. We use a dual-metric approach to measure performance: first, by checking if the target bitstring was identified, and second, by calculating the Fidelity Error (\mathcal{F}) to see how well it was identified. This provides a high-resolution view of how hardware noise destroys constructive interference, offering deeper insights than standard aggregate metrics like Quantum Volume.

Our experimental results on IQM’s superconducting and AQT’s trapped-ion systems reveal a clear capability horizon for current NISQ devices. While both platforms successfully identified peaks for small- to medium-scale circuits, signal integrity rapidly decayed as entanglement increased with depth and qubit count.

Notably, our findings uncover a significant gap between the requirements for a verifiable quantum advantage demonstration and the current operational limits of commercial hardware. For the PRC architecture used in this paper, the computational demands of maintaining a sharp peak across a 20-qubit brick-wall structure proved to be a formidable stress test, often exceeding the coherence and gate-fidelity budgets of state-of-the-art machines. Consequently, this work provides a

practical reality check: PRCs designed for quantum advantage are currently too complex for NISQ hardware at scale. The issue is not the circuit design itself, but rather how hardware noise “washes out” the interference patterns these algorithms require.

Future work has to focus on scaling PRC generation. While our current optimization step works for small qubit counts, larger circuits will require more efficient methods, such as block-based optimization. We also plan to explore “super-peaked” circuits, which trade randomness for a stronger signal to better test the limits of next-generation processors.

ACKNOWLEDGMENTS

The authors gratefully acknowledge the use of the quantum systems QExa20 and AQT20, operated by the Leibniz Supercomputing Centre (LRZ) in Garching, Germany, providing the computational resources for this work.

Parts of this work were funded by the Munich Quantum Valley (MQV) initiative and the Q-DESSI project. Hardware operations and associated software stack projects were supported by the German Federal Ministry of Research, Technology and Space (BMFTR) and the Bavarian State Ministry of Science and the Arts (StMWK).

REFERENCES

- [1] J. M. Gambetta, J. M. Chow, and M. Steffen, “Building logical qubits in a superconducting quantum computing system,” *npj quantum information*, vol. 3, no. 1, p. 2, 2017. [Online]. Available: <https://doi.org/10.1038/s41534-016-0004-0>
- [2] C. D. Bruzewicz, J. Chiaverini, R. McConnell, and J. M. Sage, “Trapped-ion quantum computing: Progress and challenges,” *Applied physics reviews*, vol. 6, no. 2, 2019. [Online]. Available: <https://doi.org/10.1063/1.5088164>
- [3] L. Henriot, L. Beguin, A. Signoles, T. Lahaye, A. Browaeys *et al.*, “Quantum computing with neutral atoms,” *Quantum*, vol. 4, p. 327, 2020. [Online]. Available: <https://doi.org/10.22331/q-2020-09-21-327>
- [4] D. E. Browne and T. Rudolph, “Resource-efficient linear optical quantum computation,” *Physical Review Letters*, vol. 95, no. 1, p. 010501, 2005. [Online]. Available: <https://doi.org/10.1103/PhysRevLett.95.010501>
- [5] S. Aaronson and Y. Zhang, “On verifiable quantum advantage with peaked circuit sampling,” *arXiv preprint arXiv:2404.14493*, 2024. [Online]. Available: <https://doi.org/10.48550/arXiv.2404.14493>
- [6] Y. Zhang, “Complexity and hardness of random peaked circuits,” *arXiv preprint arXiv:2510.00132*, 2025. [Online]. Available: <https://doi.org/10.48550/arXiv.2510.00132>
- [7] E. Pelofske, A. Bärttschi, and S. Eidenbenz, “Quantum volume in practice: What users can expect from NISQ devices,” *IEEE Transactions on Quantum Engineering*, vol. 3, pp. 1–19, 2022. [Online]. Available: <https://doi.org/10.1109/TQE.2022.3184764>
- [8] H. Heimonen, A. Auer, V. Bergholm, I. de Vega, and M. Möttönen, “Quantum computing at IQM,” in *Impact of Scientific Computing on Science and Society*. Springer, 2023, pp. 373–393. [Online]. Available: https://doi.org/10.1007/978-3-031-29082-4_22
- [9] I. Pogorelov, T. Feldker, C. D. Marciniak, L. Postler, G. Jacob *et al.*, “Compact ion-trap quantum computing demonstrator,” *PRX quantum*, vol. 2, no. 2, p. 020343, 2021. [Online]. Available: <https://doi.org/10.1103/PRXQuantum.2.020343>
- [10] A. Li, S. Stein, S. Krishnamoorthy, and J. Ang, “Qasmbench: A low-level quantum benchmark suite for NISQ evaluation and simulation,” *ACM Transactions on Quantum Computing*, vol. 4, no. 2, pp. 1–26, 2023. [Online]. Available: <https://doi.org/10.1145/3550488>
- [11] T. Proctor, K. Young, A. D. Baczewski, and R. Blume-Kohout, “Benchmarking quantum computers,” *Nature Reviews Physics*, vol. 7, no. 2, pp. 105–118, 2025. [Online]. Available: <https://doi.org/10.1038/s42254-024-00796-z>
- [12] J. M. Lorenz, T. Monz, J. Eisert, D. Reitzner, F. Schopfer *et al.*, “Systematic benchmarking of quantum computers: Status and recommendations,” *arXiv preprint arXiv:2503.04905*, 2025. [Online]. Available: <https://doi.org/10.48550/arXiv.2503.04905>
- [13] A. W. Cross, L. S. Bishop, S. Sheldon, P. D. Nation, and J. M. Gambetta, “Validating quantum computers using randomized model circuits,” *Physical Review A*, vol. 100, no. 3, p. 032328, 2019. [Online]. Available: <https://doi.org/10.1103/PhysRevA.100.032328>
- [14] A. Wack, H. Paik, A. Javadi-Abhari, P. Jurcevic, I. Faro *et al.*, “Quality, speed, and scale: Three key attributes to measure the performance of near-term quantum computers,” *arXiv preprint arXiv:2110.14108*, vol. 2110, 2021. [Online]. Available: <https://doi.org/10.48550/arXiv.2110.14108>
- [15] M. Amico, H. Zhang, P. Jurcevic, L. S. Bishop, P. Nation *et al.*, “Defining best practices for quantum benchmarks,” in *2023 IEEE International Conference on Quantum Computing and Engineering (QCE)*, vol. 1. IEEE, 2023, pp. 692–702. [Online]. Available: <https://doi.org/10.1109/QCE57702.2023.00084>
- [16] L. Kong, F. Zhang, and J. Chen, “Benchmarking fault-tolerant quantum computing hardware via QLOPS,” *ACM Transactions on Quantum Computing*, 2025. [Online]. Available: <https://doi.org/10.1145/3797968>
- [17] E. Magesan, J. M. Gambetta, and J. Emerson, “Scalable and robust randomized benchmarking of quantum processes,” *Physical Review Letters*, vol. 106, no. 18, May 2011. [Online]. Available: <http://dx.doi.org/10.1103/PhysRevLett.106.180504>
- [18] A. Silva and E. Greplova, “Hands-on introduction to randomized benchmarking,” *SciPost Physics Lecture Notes*, Jul. 2025. [Online]. Available: <http://dx.doi.org/10.21468/SciPostPhysLectNotes.97>
- [19] T. Proctor, S. Seritan, K. Rudinger, E. Nielsen, R. Blume-Kohout, and K. Young, “Scalable randomized benchmarking of quantum computers using mirror circuits,” *Physical Review Letters*, vol. 129, no. 15, Oct. 2022. [Online]. Available: <http://dx.doi.org/10.1103/PhysRevLett.129.150502>
- [20] T. Lubinski, S. Johri, P. Varosy, J. Coleman, L. Zhao *et al.*, “Application-oriented performance benchmarks for quantum computing,” *IEEE Transactions on Quantum Engineering*, vol. 4, pp. 1–32, 2023. [Online]. Available: <https://doi.org/10.1109/TQE.2023.3253761>
- [21] J. R. Finzgar, P. Ross, L. Hölscher, J. Klepsch, and A. Luckow, “Quark: A framework for quantum computing application benchmarking,” in *2022 IEEE International Conference on Quantum Computing and Engineering (QCE)*, 2022, pp. 226–237.
- [22] O. G. Udalov, “A method for constructing quasi-random peaked quantum circuits,” *arXiv preprint arXiv:2508.07491*, 2025. [Online]. Available: <https://doi.org/10.48550/arXiv.2508.07491>
- [23] H. Gharibyan, M. Z. Mullath, N. E. Sherman, V. P. Su, H. Tepanyan, and Y. Zhang, “Heuristic quantum advantage with peaked circuits,” 2025. [Online]. Available: <https://doi.org/10.48550/arXiv.2510.25838>
- [24] A. Javadi-Abhari, M. Treinish, K. Krsulich, C. J. Wood, J. Lishman *et al.*, “Quantum computing with qiskit,” *arXiv preprint arXiv:2405.08810*, 2024. [Online]. Available: <https://doi.org/10.48550/arXiv.2405.08810>
- [25] L. Burgholzer, J. Echavarría, P. Hopf, Y. Stade, D. Rovara *et al.*, “The munich quantum software stack: Connecting end users, integrating diverse quantum technologies, accelerating HPC,” *arXiv preprint arXiv:2509.02674*, 2025. [Online]. Available: <https://doi.org/10.48550/arXiv.2509.02674>